

Fracture Mechanisms of Rock-Concrete Interface: Experimental and Numerical

Wei Dong¹; Zhimin Wu²; Xiangming Zhou, M.ASCE³

¹Associate Professor, State Key Laboratory of Coastal and Offshore Engineering, Dalian University of Technology, Dalian 116024, P. R. China (corresponding author). E-mail: dongwei@dlut.edu.cn.

²Professor, State Key Laboratory of Coastal and Offshore Engineering, Dalian University of Technology, Dalian 116024, P. R. China.

³Senior lecturer, Department of Mechanical, Aerospace and Civil Engineering, Brunel University, London, UB8 3PH, UK & Haitian Visiting Professor, State Key Laboratory of Coastal and Offshore Engineering, Dalian University of Technology, Dalian 116024, P. R. China.

ABSTRACT

Uniaxial tension and three-point bending tests are conducted on rock-concrete composite specimens with artificial grooving or natural interfaces to investigate the interface mechanics and fracture properties to establish an interface tension-softening constitutive law between concrete and rock for analyzing fracture failure of rock-concrete structures. Tensile strength, fracture energy and initial fracture toughness of a rock-concrete interface are obtained from experiment. Based on the load-displacement curves measured in the three-point bending test, the energy dissipation at a rock-concrete interface is derived using the modified J-integral method. Further, through enforcing a balance between energy dissipation and energy generated by fictitious cohesive forces acting on the fracture process zone, the tension-softening constitutive law of a rock-concrete interface is established, which takes into account the effects of fracture energy and tensile strength of an interface. For the sake of

26 practical applications, the tension-softening constitutive expression is simplified as a bilinear
27 function. Finally, the crack propagation process of a series of concrete-rock composite beams
28 is simulated numerically based on a nonlinear fracture mechanics theory by introducing a
29 crack propagation criterion. The predicted load vs. crack mouth opening displacement
30 (*P-CMOD*) curves show a reasonable agreement with the experimental ones, verifying the
31 tension-softening constitutive law for a rock-concrete interface derived in this study.

32 **Author keywords: rock-concrete interface; tension-softening constitutive; degree of**
33 **roughness; nature surface; fracture.**

34

35 **Introduction**

36 The interface between concrete and rock is usually considered as the weakest in concrete
37 structures built on a rock foundation, e.g. concrete dams. In stability analyses of structures
38 aiming at sliding along a pre-existing compressed discontinuity (Javanmardi et al. 2005),
39 crack initiation and propagation along the interface (Kishen and Singh 2001; Zhong et al.
40 2014) are understudied topics. It is well known that crack development under hydrostatic
41 pressure results in the significant change in the failure behavior of a concrete dam on a rock
42 foundation. Therefore, a better understanding of the rock-concrete interface bond mechanism
43 and its fracture behavior is significant to ensure the safety and durability of a dam under
44 service load conditions.

45 In order to investigate the interaction between rock and concrete at their interface,
46 experimental studies on interface fracture properties have been conducted, focusing on the
47 fracture toughness (Yang et al. 2008), energy release rate (Kishen and Saouma 2004; Sujatha
48 and Kishen 2003) and cracking pattern (Slowik et al. 1998; Zhong et al. 2014) etc. Those
49 experimental results indicated that the fracture property of a rock-concrete interface is
50 dependent on the degree of roughness at the interface. However, it should be noted that the

51 aforementioned experimental investigations mainly focused on the fracture properties of the
52 rock-concrete interface under various stress fields, rather than on the effects of the interfacial
53 bond on fracture properties of the interface. Therefore, in those studies, either the rock
54 surfaces were treated to be very rough to obtain an adequate bond between the rock and
55 concrete, or the rock was replaced by high strength concrete, also allowing the same
56 satisfactory bond quality to be achieved. Previously, no research has been conducted on the
57 effects of a rock-concrete interface on the fracture behavior of rock-concrete structures. Also,
58 in order that the assumption of the idealized cohesive interface is applicable, rock with
59 smooth surfaces were used in the experiment's sample preparation to reduce the roughness
60 effect (Tian et al. 2014). In fact, the rock-concrete interfacial bond property mainly depends
61 on adhesion between rock and concrete, cohesion in the substrate concrete, friction, and
62 aggregate interlocking (Zhang et al. 2013). Therefore, the degree of roughness at the interface
63 significantly affects the failure behavior of rock-concrete joints. Particularly for rock with a
64 natural surface in real engineering projects in the field, the fracture properties of a
65 rock-concrete interface should be investigated for structural safety because contrary to other
66 researches, the bond between rock and concrete is actually not perfect. Therefore, it is
67 necessary to evaluate the influence of the degree of roughness on the fracture properties of a
68 rock-concrete interface and study the fracture behavior in the case of a natural interface.

69 Meanwhile, the softening constitutive law is one of the key fracture properties of a
70 rock-concrete interface and based on which it is possible to evaluate the bond failure behavior
71 of rock-concrete composite structures in the stage of post-peak loading. Similar to
72 cement-based materials, a rock-concrete interface exhibits typical quasi-brittle behaviors, i.e.
73 there is a fracture process zone (FPZ) ahead of the interface crack, which features strain
74 softening and strain localization behavior. For the purpose of simplification, some researchers
75 (Sujatha and Kishen 2003; Yang et al. 2008) ignored the FPZ, employing only the linear

76 elastic fracture theory to approximatively analyze the fracture behavior in a rock-concrete
77 interface. However, this measure is inadequate at capturing the nonlinear response of a
78 structure because without an FPZ, a crack will directly go into an unstable propagation stage
79 once it initiates. By comparing the linear and nonlinear fracture methods, Červenka et al
80 (1998) pointed out that compared to linear analysis, the critical fracture energy based on
81 nonlinear analysis can be increased by about 20%. Therefore, the nonlinear fracture
82 mechanics is more appropriate in the analysis of rock-concrete interface fracture.

83 Due to the introduction of FPZ in the nonlinear fracture analysis, calculation of fracture
84 parameters in different crack propagation stages and investigation of the crack propagation
85 process in a rock-concrete interface becomes more feasible and applicable. According to the
86 fictitious crack model proposed by Hillerborg (1976), the tension-softening behaviors of FPZ
87 in cement-based materials can be described using the normal stress acting on crack surface
88 vs. crack opening displacement. So far, several expressions have been proposed for
89 determining the softening stress (σ)-crack opening displacement (w) relationship for concrete,
90 which include linear (Hillerborg et al. 1976), bilinear (Petersson 1981) and nonlinear ones
91 (Foote et al. 1986). The fictitious crack model has been gradually accepted by scientific and
92 engineering communities and now is widely used for simulation of concrete fracture
93 propagation (Wu et al. 2013). It should be noted that even for concrete, there are
94 controversial issues in determining the shape of the softening curve. As an example of the
95 bilinear relationship, the tensile stress at the intersection point was recommended as $0.15 f_t$ by
96 CEB-FIP model code in 1990, $1/3 f_t$ by Peterson (1981) and $0.25 f_t$ by Wittmann (1988) all
97 based on experimental results. Here, f_t denotes the uniaxial tensile strength of concrete. For
98 concrete-to-concrete interface fracture, the tension softening and nonlinear fracture properties
99 between different strengths of concrete have been investigated experimentally by Shah et al.
100 (2011; 2010). However, in cases of a rock-concrete interface, to the best of the authors'

101 knowledge, no formulized tension-softening relationship based on experimental results has
102 been reported. In the few studies on crack propagation along the rock-concrete interface
103 (Alberto and Valente 2013; Barpi and Valente 2010; Zhong et al. 2014), the formula
104 constitutive relationship based on concrete materials was adopted to describe the softening
105 behavior of the interface. Therefore, from the view of exploring the rock-concrete interface
106 bond mechanism, it is significant to study the interfacial fracture behavior through
107 experiment and to obtain the tension constitutive relationship for design and analysis of
108 rock-concrete structures. It is expected to derive a universal interfacial tension-softening
109 constitutive model with respect to the varied degrees of roughness, particularly for the
110 interface with a natural rock surface.

111 In line with this, the objective of this paper is to focus on the rock-concrete interface fracture
112 properties and tension-softening constitutive model subjected to mode I fracture. Firstly,
113 experimental studies, including direct tensile test and three-point bending beam test, are
114 carried out to investigate the interfacial fracture toughness, fracture energy and bond strength,
115 with respect to the rock-concrete interfaces with different degrees of roughness. Further,
116 based on experimental results of the three-point bending test of concrete beams, a
117 tension-softening constitutive model is derived, which takes into account the effects of
118 interfacial fracture energy and tensile strength of interface. Finally, the numerical simulation
119 aiming at the interfacial crack propagation process is conducted to validate the derived
120 tension constitutive model through comparing the load vs. crack mouth opening displacement
121 (*P-CMOD*) curves obtained in numerical and experimental studies.

122

123 **Experimental Program**

124 *Specimen Preparation*

125 Two types of specimens were tested in this study. One was that of the 100 mm × 100 mm ×
126 200 mm prisms for the direct tensile test. The other was that of the 100 mm × 100 mm × 500
127 mm (width×depth×length) beams with a 400 mm-span for three-point bending test. All
128 specimens consisted of two geometrically identical blocks, which are rock and concrete
129 block, respectively. The rock used to make the composite specimens in this study is granite
130 and is produced in Shandong Province, China. The concrete mix proportion for this study was
131 1:0.62:1.8:4.2 (cement: water: sand: aggregate) by weight and the maximum aggregate size
132 was 10 mm. Rock specimens were placed inside moulds and concrete mixtures were cast in
133 the remaining mould space. After curing in sealed moulds for two days, the composite
134 specimens were de-moulded and moved into a curing room with 23°C and 90% RH for
135 continued curing until 28 days. The measured material properties are listed in Table 1, in
136 which E_t , ν , and f_c denote Young modulus, Poisson's ratio and uniaxial compressive strength
137 of concrete, respectively.

138

139 *Surface Roughness Characterization*

140 To study the effect of interfacial roughness on fracture properties and bond strength, two
141 kinds of rough surfaces of rock were investigated, either with artificial grooves or natural
142 joint. The roughness of interface was achieved by varying the grooving depth and groove
143 number at the rock surface. As shown in Fig. 1, there were four kinds of grooving numbers
144 investigated in this study, i.e. $n=0, 2, 4$ and 6 , and the depth of grooves is varied as 2 mm, 4
145 mm and 6 mm. Here, n denotes the number of groove branches. The roughness of interface
146 was quantified by the sand filling method. Fine sand was filled in the artificial groove until it
147 reached the same level of the surface of an un-cut portion of the rock specimen. Then, the
148 degree of roughness R_a was calculated from the following equation:

$$149 \quad R_a = V/A \quad (1)$$

150 where V is the volume of sand filled in the groove, and A is the cross-section area of the
151 specimen. It should be noted that, in the case of pre-notched specimens, A is the
152 cross-sectional area of a rock specimen above the pre-notch.

153 The natural surface of rock can be obtained from the three-point bending test of rock beams
154 with/without a notch. Once a rock beam is broken into two halves under bending, each half
155 will have a natural surface, which is shown in Fig. 2. Concrete will then be cast in a mould
156 containing the broken rock to make a rock-concrete composite sample for testing in this
157 study. For the prisms (DT series) and three-point bending beams (with natural interface
158 denoted as TPB series and with artificial grooving interface as TPB-A series), there were in
159 total ten different degrees of roughness investigated ranging from 0 mm to 1.15 mm in this
160 study, which are listed in Table 1. For the TPB-A series specimens with artificial grooves, the
161 initial crack ratio a_0/D was set as 0.3. In the case of natural surface, a_0/D was varied as 0.2,
162 0.3, 0.4, 0.5, and 0.6. Here, a_0 is the initial crack length, and D is the depth of the beam. For
163 instance, the specimen number “DT2-4” denotes a direct tension rock-concrete composite
164 sample of artificial grooving interface where $n=2$ and grooves are 4 mm deep; the specimen
165 “TPB-A 6-2” denotes a three-point bending beam with an artificial grooving interface where
166 $n=2$ and grooves are 6 mm deep; the specimen “TPB 3” denotes a three-point bending beam
167 with a natural interface and $a_0/D=0.3$.

168

169 ***Direct Tensile Test***

170 In this study, a direct tensile test was conducted to measure the uniaxial tensile strength of
171 the rock-concrete interface, as shown in Fig. 3. In order to achieve a homogeneous tensile
172 stress distribution at the interface, four clip gauges were set to monitor the relative vertical
173 displacement of the top and bottom surfaces of a rock-concrete composite prism, which the
174 difference of displacement measured by the four clip gauges was limited within 5% at any

175 time. Clip gauges used in this study all have a range of -6 mm to 6 mm, and the loading rate
176 of the direct tensile test is 0.05 MPa/s. The uniaxial tensile strength, f_t , is calculated from the
177 following equation:

$$178 \quad f_t = P_{max}/A \quad (2)$$

179 where, P_{max} is the peak load, and A is the interfacial area.

180 The cracking patterns for the artificial grooving and natural interfaces at failure are
181 presented in Fig. 4. It can be seen from this figure that the treatment by artificial
182 grooving can provide higher bond effect between concrete and rock. For the specimens
183 with an artificial grooving interface, the failure in the artificial grooving interface is due
184 to concrete in tension while the failure on the smooth surface between concrete and rock
185 is due to the weak bond. In the case of specimens with natural interface, the failure
186 between the concrete and rock is only due to the weak bond.

187

188 ***Three-Point Bending Test***

189 A closed loop servo-controlled testing machine with a capacity of 250 kN was used for the
190 three-point bending test. The loading-point displacement of composite specimens and their
191 crack mouth opening displacement were measured by two clip gauges. To obtain the crack tip
192 opening displacement and crack propagation process, four clip gauges were mounted
193 equidistantly from the tip of the pre-crack to the top of a composite beam. To measure the
194 initial cracking load, four strain gauges were attached vertically 10mm apart in front of the
195 precast notch on both sides of a beam specimen. The experimental setup for the three-point
196 bending test is shown in Fig. 5. When a crack initiates and starts to propagate, the value
197 measured by the strain gauge will decrease suddenly and significantly due to the release of
198 fracture energy. Therefore, the initial cracking load can be obtained according to the variation
199 of the strain at the tip of a pre-notch (See Fig. 6).

200 In this study, the displacement extrapolation method was used to calculate the stress intensity
 201 factors K_1 and K_2 of the bi-material interface crack through the relative crack surface
 202 displacements δ_x and δ_y , as shown in the following equations (Nagashima et al. 2003):

$$203 \quad K_1 = C \lim_{r \rightarrow 0} \sqrt{\frac{2\pi}{r}} \left[\delta_y (\cos Q + 2\varepsilon \sin Q) + \delta_x (\sin Q - 2\varepsilon \cos Q) \right] \quad (3)$$

$$204 \quad K_2 = C \lim_{r \rightarrow 0} \sqrt{\frac{2\pi}{r}} \left[\delta_y (\cos Q + 2\varepsilon \sin Q) - \delta_x (\sin Q - 2\varepsilon \cos Q) \right] \quad (4)$$

205 where

$$206 \quad C = \frac{2 \cosh(\varepsilon\pi)}{(\kappa_1 + 1)/\mu_1 + (\kappa_2 + 1)/\mu_2} \quad (5)$$

$$207 \quad Q = \varepsilon \ln r \quad (6)$$

$$208 \quad \varepsilon = \frac{1}{2\pi} \ln \left(\frac{\frac{\kappa_1 + 1}{\mu_1} \frac{\mu_2}{\kappa_2 + 1}}{\frac{\mu_2}{\mu_1}} \right) \quad (7)$$

$$209 \quad \mu_i = \frac{E_i}{2(1+\nu_i)} \quad (i=1, 2) \quad (8)$$

$$210 \quad \kappa_i = (3-\nu_i)/(1+\nu_i) \quad (\text{Plane stress})$$

$$211 \quad = (3-\nu_i) \quad (\text{Plane strain}) \quad (9)$$

212 It should be noted that stress intensity factors K_1 and K_2 can be denoted as K_1^{ini} and K_2^{ini}
 213 when δ_x and δ_y in Eqs. 3 and 4 are caused by the initial cracking load.

214

215 **Test Results and Discussions**

216 *Effect of Roughness on Mechanical and Fracture Properties of Artificial Grooving* 217 *Interface*

218 Figs. 7 (a) and (b) illustrate the relationships of uniaxial tensile strength f_t and initial fracture
 219 toughness K_1^{ini} , respectively, with respect to the interfacial degree of roughness, R_a . The

220 average experimental results for the specimens with an artificial grooving interface are listed
221 in Table 2. According to these, both f_t , and K_1^{ini} increase with the rise of R_a in the case of an
222 artificial grooving interface. In the case of plain concrete, the average values of f_t , and K_1^{ini}
223 obtained from experiment are 2.96 MPa and $0.49 \text{ MPa}\cdot\text{m}^{1/2}$, respectively. It indicates that,
224 although the increase of interface roughness enhances the cracking resistance, f_t and K_1^{ini} of a
225 concrete-rock interface are less than their corresponding value of concrete when R_a reaches
226 its maximum value, i.e. $R_a=1.15$ mm in this study. Meanwhile, in the case of a natural
227 interface and with $a_0/D=0.3$, the average values of f_t , and K_1^{ini} obtained from experiment are
228 1.371 MPa and $0.19 \text{ MPa}\cdot\text{m}^{1/2}$, respectively, which corresponds to an R_a value of about 0.6
229 mm and 0.2 mm, respectively. Judging from the initial fracture toughness, the natural
230 interface shows a very weak bond between concrete and rock, i.e. K_1^{ini} of a nature interface
231 is only greater than that of the smooth interface. Although the scenario of f_t is different, it can
232 be reasonably concluded that the rough surface of a nature interface increases the bonding
233 area, which is not considered in the calculation of f_t . Therefore, it is necessary to increase the
234 degree of roughness at the interface for the purpose of enhancing the crack resistance and
235 bonding effect.

236

237 *Effect of a_0/D on Fracture Properties of Natural Interface*

238 Figs. 8 (a) and (b) illustrate the relationships of initial fracture toughness K_1^{ini} and fracture
239 energy G_f , respectively, with respect to initial crack ratio, a_0/D . The average values of the
240 relevant parameters from experiment for specimens with a natural interface are listed in Table
241 3. It indicates that K_1^{ini} and G_f do not vary significantly with respect to a_0/D . Therefore,
242 K_1^{ini} and G_f of a rock-concrete natural interface can be regarded as being independent from
243 a_0/D , which is the same conclusion drawn from concrete materials (Xu and Reinhardt 1999a;

244 Xu and Reinhardt 1999b). Compared with the corresponding values of plain concrete
245 investigated in this study, i.e. $K_1^{ini}=0.49 \text{ MPa}\cdot\text{m}^{1/2}$ and $G_f=87 \text{ N/m}$, it can be concluded that
246 the natural interface shows lower crack resistance and a weaker energy absorbing capacity
247 during crack propagation.

248

249 **Tension-Softening Constitutive Law of Rock-Concrete Interface**

250 To get the tension-softening diagram after the peak interfacial stress, Niwa et al. (1998)
251 proposed a modified J-integral method, which can consider crack propagation and remove the
252 elastic displacement of the beam due to crack initiation. Using this method, Dai et al. (2003)
253 and Zhang et al. (2013) derived the tension-softening diagrams for FRP-concrete and
254 polymer cement mortar-concrete interfaces, respectively. The J-integral is defined as the
255 energy available for crack propagation $E(\delta)$, which can be interpreted as the total absorbed
256 energy of a cracked specimen minus the released elastic energy during the unloading process
257 (see Fig. 9). If both the unloading and reloading paths can be assumed as linear, $E(\delta)$ can be
258 written as Equation (10):

$$259 \quad E(\delta) = \int_0^{\delta} P(\delta) d\delta - \frac{1}{2} P(\delta) (\delta - \delta_p) \quad (10)$$

260 where δ is the displacement under a certain load and δ_p is the residual displacement at a fully
261 unloaded state, which can be obtained from the unloading and reloading process shown in
262 Fig. 9. As an example, Figs. 10 (a) to (d) illustrate the P - δ curves of specimen TPB-A 4-2-3
263 and TPB-A 6-4-1 with the artificial grooving interface, and specimen TPB 2-5 and TPB 5-5
264 with the natural interface. Based on the operations of unloading and reloading for all
265 specimens, the δ - δ_p relationship from experiment can be derived through normalization using
266 the maximum displacement δ_{max} , which is shown in Fig. 11. For the two types of
267 rock-concrete interface, δ - δ_p relationship can be formulated as Equation (11):

268
$$\delta_p/\delta_{max}=(\delta/\delta_{max})^{1.375} \quad (11)$$

269 If the energy $E(\delta)$ is used to drive crack propagation, the tension-softening relationship can
 270 be derived as Equation (12) (Niwa et al. 1998):

271
$$\sigma(w) = \frac{1}{ab} (2E'(w) + wE''(w)) \quad (12)$$

272 where $E'(w)$ and $E''(w)$ are the first and second derivatives of energy E , a and b is the
 273 propagated crack length and beam width, respectively, σ is the cohesive stress acting on
 274 fracture process zone and w is the crack width. The crack width at the four-equal-division
 275 points of ligament can be measured by the four clip gauges (see Fig. 5 (b)). Meanwhile, the
 276 crack propagation length can be derived by determining the fictitious crack tip, which has a 0
 277 mm crack width and can be obtained by the linear interpolation method. Based on
 278 experimental results, a - w relationship (normalized by the ligament height a_{max}) and a - δ
 279 relationship (normalized by the maximum displacement δ_{max}) can be formulated by Equations
 280 (13) and (14), respectively.

281
$$a/a_{max} = 1 - \left(1 - \sqrt{w/w_{max}}\right)^{5.76} \quad (13)$$

282
$$a/a_{max} = 1 - \left(1 - \sqrt{\delta/\delta_{max}}\right)^{5.48} \quad (14)$$

283 Then, an expression of the tension-softening constitutive law of a rock-concrete interface can
 284 be obtained by substituting equations (11), (13) and (14) into equation (12), which is shown
 285 as equation (15) (normalized by the uniaxial tensile strength f_t and the stress-free crack
 286 opening displacement w_0).

287
$$\sigma/f_t = \left(1 - \sqrt{w/w_0}\right)^q \quad (15)$$

288 It should be noted that some beam specimens failed to reach the whole post-peak stages in
 289 experiment due to the weak bonding of the rock-concrete interface. Fig. 12 illustrates the fit
 290 σ/f_t - w/w_0 relationship of all the specimens with the whole post-peak stage obtained in
 291 experiment. In equation (15), q is a non-dimensional material constant defined as a function

292 of the tensile strength f_t , fracture energy G_f and stress-free crack opening displacement w_0 ,
 293 which can be determined by fitting the experimental data as shown in Fig. 13. The fitted
 294 parameter q can be written as equation (16), in which f_t and G_f can be obtained from the
 295 experimental measurement, and w_0 can be derived according to equation (17). In this study,
 296 the stress-free crack opening displacement w_0 is approximately 0.1 mm from calculation,
 297 which was found to be independent from the roughness of interface R_a and the initial crack
 298 ratios a_0/D . Meanwhile, since the effect of R_a and a_0/D on tension-softening constitutive is
 299 reflected in equation (16), equation (15) can be used to determine the relationship of σ - w in
 300 the case of different roughness and natural interfaces of rock-concrete composite specimens.

$$301 \quad q = 0.385 \cdot f_t \cdot w_0 / G_f \quad (16)$$

$$302 \quad \int_0^{w_0} \sigma(w)dw = G_f \quad (17)$$

303 As an example, Figs. 14 (a) to (d) illustrate the derived exponential σ - w relationships of
 304 specimens TPB-A 4-2-3 and TPB-A 6-4-1 with an artificial grooving interface, and TPB 2-5
 305 and TPB 5-5 with a natural interface. Further, for the purpose of simplification in practical
 306 applications, a bilinear model, defined by the four parameters, f_t , σ_s , w_s , and w_0 , is derived to
 307 represent the real tension-softening constitutive law of a rock-concrete interface (see Fig. 14).
 308 Once the break-point, with coordinates (σ_s, w_s) is determined, the exponential
 309 tension-softening constitutive can be transformed to the bilinear one by enforcing the same
 310 fracture energy G_f . Using the method proposed by Wittmann et al. (1988), a bilinear
 311 expression of the tension-softening constitutive law is obtained as Equations (18)-(20):

$$312 \quad \sigma_s = 0.2f_t \quad (18)$$

$$313 \quad w_s = 0.8G_f/f_t \quad (19)$$

$$314 \quad w_0 = 6G_f/f_t \quad (20)$$

315 Both the exponential and bilinear curves are shown in Fig. 14 for the purpose of comparison.
 316 It can be seen that the bilinear model is a reasonable approximation of the exponential one,

317 and can reflect the variation tendency of the real σ - w relationship while a bilinear model is
318 much easier to be applied in analyzing rock-concrete elements and structures in practical
319 design with much less computational cost.

320

321 **Crack Propagation of Rock-Concrete Interface**

322 Due to the asymmetry of materials on the both sides of a crack, in the case of a
323 rock-concrete interface, it is a mixed mode fracture, rather than a simple opening mode
324 fracture under three-point bending. However, it should be noted that the stress intensity
325 factor of mode 2 is 10% less than that of mode 1, which is determined by the crack ratio
326 a/D . Meanwhile, the crack trajectory observed from experiment is always along the interface
327 until a crack propagates throughout the section. Therefore, the interfacial fracture of a
328 rock-concrete interface can be approximately regarded as dominated by mode I fracture.
329 Then, a crack propagation criterion based on the initial crack toughness is introduced to
330 determine the crack propagation in a rock-concrete interface. The crack propagation
331 criterion has been established and validated by Dong et al. (Dong et al. 2013a), and found to
332 be able to predict the whole concrete fracture process with respect to mode I fracture (Dong
333 et al. 2013a; Dong et al. 2013b; Wu et al. 2014). This criterion can be described as
334 following: a crack begins to propagate when the difference, between the stress intensity
335 factors K_1^P caused by the applied load and K_1^σ by the cohesive stress, exceeds the initial
336 fracture toughness K_1^{ini} of a rock-concrete interface. The crack propagation criterion can be
337 described as follows:

$$338 \quad K_1^P - K_1^\sigma < K_1^{ini}, \text{ crack does not propagate} \quad (21)$$

$$339 \quad K_1^P - K_1^\sigma = K_1^{ini}, \text{ crack is in the critical state} \quad (22)$$

$$340 \quad K_1^P - K_1^\sigma > K_1^{ini}, \text{ crack propagates} \quad (23)$$

341 The stress intensity factor at the crack tip is calculated based on the displacement
342 extrapolation method through the Equations (3)-(9), in which the displacements δ_x and δ_y
343 can be calculated numerically from the pre-notched three-point bending beam under an
344 external point load. According to the experimental results in this study, K_1^{ini} can be
345 calculated by measuring the initial cracking load, which depends on the roughness of an
346 artificial grooving interface, and is regarded as a material constant independent from the
347 initial crack ratio a_0/D for a natural interface between concrete and rock. The derived
348 bilinear tension-softening constitutive law in this paper is utilized to describe the
349 relationship of cohesive stress and the relative displacement of the cracking surface.
350 Therefore, K_1^σ is calculated based on the cohesive stress acting on a micro-crack, in which
351 the cohesive stress is determined through Equations (18)-(20). The details of the iterative
352 process for analyzing crack propagation based on the crack propagation criterion described
353 in Equations (21) to (23) can be found by referring to Dong et al (2013a). In this numerical
354 approach, finite element analyses were carried out using ANSYS code to simulate the crack
355 propagation process. The mechanical properties and calculated material parameters for the
356 four specimens are listed in Table 4.

357 Figs. 15 (a) to (d) illustrate the finite element mesh at various key fracture stages for
358 specimen of TPB-A 4-2-3 as an example. Meanwhile, the complete *P-CMOD* curves
359 obtained from both experiment and numerical simulation are presented in Figs. 16 (a) to (d),
360 with respect to TPB-A 4-2-3 and TPB-A 6-4-1 with an artificial grooving interface, and to
361 TPB 2-5 and TPB 5-5 with a natural interface. It can be seen that the *P-CMOD* curves
362 obtained from numerical simulation agree well with those from experiment suggesting that
363 the numerical method, together with the bilinear tension-softening constitutive law derived
364 in this paper, can be used for simulating the complete fracture process in a rock-concrete
365 interface.

366

367 **Conclusions**

368 Uniaxial tension and three-point bending tests were carried out for rock-concrete composite
369 specimens with artificial grooving and natural interfaces. The effects of degree of roughness
370 for the artificial grooving interface and initial crack ratio for the natural interface on
371 mechanics and fracture properties of rock-concrete interface were studied. Based on
372 experimental results, a tension-softening constitutive law of interface was derived and
373 employed in the numerical simulation of crack propagation process along the rock-concrete
374 interface to validate it. According to the experimental and numerical studies, the following
375 conclusions can be drawn:

- 376 1. For the artificial grooving interface, the uniaxial tensile strength f_t and initial fracture
377 toughness K_1^{ini} increase linearly with the increase of interfacial roughness R_a when R_a
378 ranges from 0 mm to 1.15 mm in this study. For the natural interface, initial fracture
379 toughness K_1^{ini} and fracture energy G_f are independent on the initial crack ratio a_0/D .
380 Meanwhile, the natural interface shows a low bond effect, whose f_t and K_1^{ini} are
381 comparable to the values of those of the artificial grooving interface with $R_a=0.6$ mm and
382 0.2 mm, respectively.
- 383 2. Using the modified J-integral method, an exponential tension-softening constitutive law
384 for rock-concrete interface was derived from experiment by taking into account fracture
385 energy, tensile strength and stress-free crack opening displacement. Further, for the sake
386 of practical applications, a simplified bilinear expression of tension-softening
387 constitutive law was proposed and verified in this research. It can be determined for
388 different interface conditions given G_f and f_t of a rock-concrete interface, regardless of
389 properties of concrete and rock, and bond condition between concrete and rock. The
390 derived constitutive law requires much less information on materials properties of

391 concrete and rock compared with many other constitutive laws for describing tension
392 softening behavior of rock-concrete interface. Very often, it is not easy to obtain those
393 required material properties of rock and concrete from experiment for those constitutive
394 laws.

395 3. A crack propagation criterion was introduced to determine crack propagation of a
396 rock-concrete interface and the whole crack propagation process of a series of
397 rock-concrete composite beams was simulated based on this crack propagation criterion.
398 Compared with the experimental results, the numerical results show a reasonable
399 agreement on the *P-CMOD* curves, indicating that the derived bilinear tension-softening
400 constitutive law is appropriate for describing the softening characteristics of a
401 rock-concrete interface in the stage of post-peak loading. A bilinear tension-softening
402 constitutive law is more convenient to be used in practical design and analysis of
403 rock-concrete composite structures.

404

405 **Acknowledgement**

406 The financial support of the, the National Natural Science Foundation of China under the
407 grant of NSFC 51478083, 51421064 and 51109026, and the fundamental research funds for
408 the Central Universities under the grant of DUT14LK06 is gratefully acknowledged.

409

410 **References**

411 Alberto, A., and Valente, S. (2013). "Asymptotic fields at the tip of a cohesive frictional crack
412 growing at the bi-material interface between a dam and the foundation rock." *Eng. Fract.*
413 *Mech.*, 108, 152-161.

414 Barpi, F., and Valente, S. (2010). "The cohesive frictional crack model applied to the analysis
415 of the dam-foundation joint." *Eng. Fract. Mech.*, 77(11), 2182-2191.

416 Červenka, J., Chandra Kishen, J. M., and Saouma, V. E. (1998). "Mixed mode fracture of
417 cementitious bimaterial interfaces: Part II: numerical simulation." *Eng. Fract. Mech.*, 60(1),
418 95-107.

419 Dai, J., Ueda, T., Hasan, M., and Sato, Y. (2003). "Mode I fracture behavior of FRP-concrete
420 interfaces." *Proc., Proc. Jpn. Concrete Inst.*, 1577-1582.

421 Dong, W., Wu, Z., and Zhou, X. (2013a). "Calculating crack extension resistance of concrete
422 based on a new crack propagation criterion." *Constr. Build. Mater.*, 38(1), 879-889.

423 Dong, W., Zhou, X., and Wu, Z. (2013b). "On fracture process zone and crack extension
424 resistance of concrete based on initial fracture toughness." *Constr. Build. Mater.*, 49(12),
425 352-363.

426 Foote, R. M. L., Mai, Y.-W., and Cotterell, B. (1986). "Crack growth resistance curves in
427 strain-softening materials." *J. Mech. Phys. Solids.*, 34(6), 593-607.

428 Hillerborg, A., Modéer, M., and Petersson, P. E. (1976). "Analysis of crack formation and
429 crack growth in concrete by means of fracture mechanics and finite elements." *Cem Concr
430 Res.*, 6(6), 773-781.

431 Javanmardi, F., Léger, P., and Tinawi, R. (2005). "Seismic structural stability of concrete
432 gravity dams considering transient uplift pressures in cracks." *Eng. Struct.*, 27(4), 616-628.

433 Kishen, J. M. C., and Saouma, V. E. (2004). "Fracture of rock-concrete interfaces: Laboratory
434 tests and applications." *ACI Struct. J.*, 101(3), 325-331.

435 Kishen, J. M. C., and Singh, K. D. (2001). "Stress intensity factors based fracture criteria for
436 kinking and branching of interface crack: application to dams." *Eng. Fract. Mech.*, 68(2),
437 201-219.

438 Nagashima, T., Omoto, Y., and Tani, S. (2003). "Stress intensity factor analysis of interface
439 cracks using X-FEM." *Int. J. Numer. Meth. Eng.*, 56(8), 1151-1173.

440 Niwa, J., Sumranwanich, T., and Tangtermsirikul, S. (1998). "New method to determine
441 tension softening curve of concrete " *Proc., Fracture Mechanics of Concrete Structures:*
442 *Proc., FRAMCOS-3, AEDIFICATIO*, 347-356.

443 Petersson, P. E. (1981). "Crack growth and development of fracture zones in plain concrete
444 and similar materials." Lund Institute of Technology, SWEDEN.

445 Shah, S. G., Bhasya, V., and Kishen, J. M. C. (2011). "Tension-Softening Properties for
446 Concrete-Concrete Interfaces." *ACI Struct. J.*, 108(6), 725-734.

447 Shah, S. G., and Kishen, J. M. C. (2010). "Nonlinear fracture properties of concrete-concrete
448 interfaces." *Mech. Mater.*, 42(10), 916-931.

449 Slowik, V., Chandra Kishen, J. M., and Saouma, V. E. (1998). "Mixed mode fracture of
450 cementitious bimaterial interfaces;: Part I: Experimental results." *Eng. Fract. Mech.*, 60(1),
451 83-94.

452 Sujatha, V., and Kishen, J. M. C. (2003). "Energy release rate due to friction at bimaterial
453 interface in dams." *J. Eng. Mech.*, 129(7), 793-800.

454 Tian, H. M., Chen, W. Z., Yang, D. S., and Yang, J. P. (2014). "Experimental and Numerical
455 Analysis of the Shear Behaviour of Cemented Concrete–Rock Joints." *Rock. Mech. Rock.*
456 *Eng.*, 48(1), 213-222.

457 Wittmann, F. H., Rokugo, K., Brühwiler, E., Mihashi, H., and Simonin, P. (1988). "Fracture
458 energy and strain softening of concrete as determined by means of compact tension
459 specimens." *Mater. Struct.*, 21(1), 21-32.

460 Wu, Z., Rong, H., Zheng, J., and Dong, W. (2013). "Numerical Method for Mixed-Mode I–II
461 Crack Propagation in Concrete." *J. Eng. Mech.*, 139(11), 1530-1538.

462 Wu, Z., Wu, X., Dong, W., Zheng, J., and Wu, Y. (2014). "An analytical method for
463 determining the crack extension resistance curve of concrete." *Mag. Concr Res.*, 66(14),
464 719-728.

465 Xu, S., and Reinhardt, H. (1999a). "Determination of double-Determination of double-K
466 criterion for crack propagation in quasi-brittle fracture Part I: experimental investigation of
467 crack propagation." *Int. J. Fracture.*, 98(2), 111-149.

468 Xu, S., and Reinhardt, H. W. (1999b). "Determination of double-K criterion for crack
469 propagation in quasi-brittle fracture, Part II: Analytical evaluating and practical measuring
470 methods for three-point bending notched beams." *Int. J. Fracture.*, 98(2), 151-177.

471 Yang, S., Song, L. I., Li, Z. H. E., and Huang, S. (2008). "Experimental investigation on
472 fracture toughness of interface crack for rock/concrete." *Int. J. Mod. Phys. B*, 22(31n32),
473 6141-6148.

474 Zhang, D., Ueda, T., and Furuuchi, H. (2013). "Fracture Mechanisms of Polymer Cement
475 Mortar: Concrete Interfaces." *J. Eng. Mech.*, 139(2), 167-176.

476 Zhong, H., Ooi, E. T., Song, C., Ding, T., Lin, G., and Li, H. (2014). "Experimental and
477 numerical study of the dependency of interface fracture in concrete–rock specimens on mode
478 mixity." *Eng. Fract. Mech.*, 124-125, 287-309.

479 **Appendix I Table**

480

481 **Table 1. Materials Properties of Concrete and Rock**

Material	Density (kN/m ³)	E_t (GPa)	ν	f_c (MPa)	f_t (MPa)	K_1^{ini} (MPa·m ^{1/2})	G_f (N/m)
Concrete	2400	30.26	0.238	36.13	2.88	0.49	87
Rock	2668	64.39	0.198	119.2	8.65	1.0	119.7

482

483 **Table 2. Results of Direct Tensile and Three-point Bending Tests for Artificial Grooving**
484 **Interfaces**

Specimen	\bar{R}_a (mm)	\bar{f}_t (MPa)	Specimen	\bar{R}_a (mm)	\bar{K}_1^{ini} (MPa·m ^{1/2})	\bar{K}_2^{ini} (MPa·m ^{1/2})
DT 0-0	0	0.426	TPB-A 0-0	0.000	0.259	-0.0174
DT 2-2	0.199	0.528	TPB-A 2-2	0.197	0.248	-0.0167
DT 2-4	0.386	0.877	TPB-A 2-4	0.400	0.296	-0.0199
DT 2-6	0.608	1.362	TPB-A 2-6	0.507	0.203	-0.0136
DT 4-2	0.351	0.846	TPB-A 4-2	0.401	0.320	-0.0215
DT 4-4	0.710	1.088	TPB-A 4-4	0.786	0.319	-0.0214
DT 4-6	1.146	1.504	TPB-A 4-6	1.009	0.504	-0.0339
DT 6-2	0.356	1.173	TPB-A 6-2	0.467	0.309	-0.0208
DT 6-4	0.944	1.252	TPB-A 6-4	0.919	0.427	-0.0287
DT 6-6	1.090	1.288	TPB-A 6-6	1.124	0.399	-0.0268

485

486 **Table 3. Results of Three-point Bending Test for Specimens with Natural Interfaces**

Specimen	a_0/D	\bar{P}_{ini} (kN)	\bar{P}_{max} (kN)	\bar{K}_1^{ini} (MPa·m ^{1/2})	\bar{K}_2^{ini} (MPa·m ^{1/2})	\bar{G}_f (N/m)
TPB 2	0.2	1.35	1.60	0.20	-0.0095	16.58
TPB 3	0.3	0.97	1.10	0.19	-0.0125	12.87
TPB 4	0.4	0.96	1.15	0.24	-0.019	11.55
TPB 5	0.5	0.88	1.08	0.27	-0.0226	19.18
TPB 6	0.6	0.54	0.66	0.25	-0.0219	21.11

487

488 **Table 4. Mechanical Properties and Calculated Parameters Used in Simulation**

Concrete	$E_t=30.26$ GPa, $\nu=0.238$	TPB-A 4-2-3	$f_t=0.528$ MPa, $G_f=19.47$ N/m $K_1^{ini}=0.326$ MPa·m ^{1/2} , $a_0=32$ mm
Rock	$E_t=64.39$ GPa, $\nu=0.198$	TPB-A 6-4-1	$f_t=1.252$ MPa, $G_f=28.81$ N/m $K_1^{ini}=0.399$ MPa·m ^{1/2} , $a_0=34$ mm
Specimen size	Width×Depth×Length= 100mm × 100mm × 500mm	TPB 2-5	$f_t=1.371$ MPa, $G_f=19.72$ N/m $K_1^{ini}=0.226$ MPa·m ^{1/2} , $a_0=20$ mm
Crack increment	$\Delta a=2$ mm	TPB 5-5	$f_t=1.371$ MPa, $G_f=24.66$ N/m $K_1^{ini}=0.31$ MPa·m ^{1/2} , $a_0=50$ mm

489

490 **Captions of figures**

491 **Fig. 1.** Roughening of rock surface at the interface: (a) $n=0$; (b) $n=2$; (c) $n=4$; and (d) $n=6$

492 **Fig. 2.** Test for obtaining the natural surface of rock: (a) Test set-up; and (b) Natural surface

493 **Fig. 3.** Direct tensile test: (a) Vertical view; and (b) Plan view

494 **Fig. 4.** Cracking patterns of rock-concrete interface: (a) Artificial grooving interface; and
495 (b) Natural interface

496 **Fig. 5.** Three-point bending beam test setup: (a) Set-up for measurement of loading-point
497 displacement; and (b) Set-up for measurement of crack opening displacement

498 **Fig. 6.** Strain variation of concrete around crack tip

499 **Fig. 7.** Effects of interface roughness R_a on f_t and K_I^{ini} : (a) Uniaxial tensile strength f_t ; and (b)
500 Initial fracture toughness K_I^{ini}

501 **Fig. 8.** Effects of initial crack ratios a_0/D on f_t and K_I^{ini} : (a) Initial fracture toughness K_I^{ini} ;
502 and (b) Fracture energy G_f

503 **Fig. 9.** Illustration of the modified J integral method

504 **Fig. 10.** Load-displacement relationship: (a) TPB-A 4-2-3; (b) TPB-A 6-4-1; (c) TPB 2-5;
505 and (d) TPB 5-5

506 **Fig. 11.** $\delta_p/\delta_{max}-\delta/\delta_{max}$ relationship

507 **Fig. 12.** $\sigma/f_t-w/w_0$ relationship

508 **Fig. 13.** Curve fitting for the material constant q

509 **Fig. 14.** Tension-softening constitutive law of rock-concrete interface: (a) TPB-A 4-2-3; (b)
510 TPB-A 6-4-1; (c) TPB 2-5; and (d) TPB 5-5

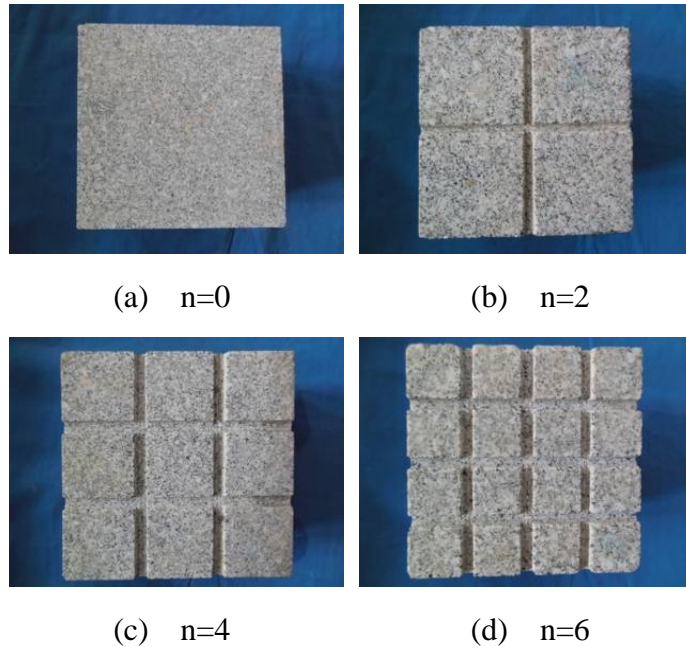
511 **Fig. 15.** Mesh and deformation of different fracture stages for specimen of TPB-A 4-2-3: (a)
512 Crack initiation; (b) Critical crack propagation (Peak load); (c) The 15th increase step
513 ($\Delta a=30\text{mm}$); and (d) Failure of specimens

514 **Fig. 16.** Comparison of *P-CMOD* curves between experimental and numerical: (a) TPB-A
515 4-2-3; (b) TPB-A 6-4-1; (c) TPB 2-5; and (d) TPB 5-5

516

517

518



519

520

521

522

523

524

525

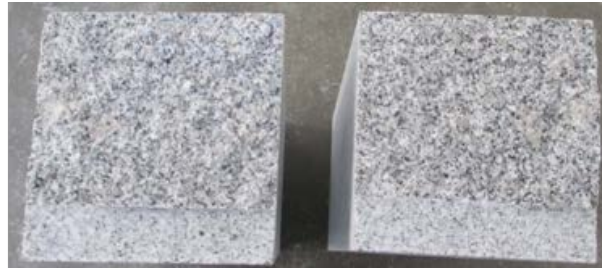
Fig. 1. Roughness of rock surface at the interface

526



527

(a) Test set-up



528

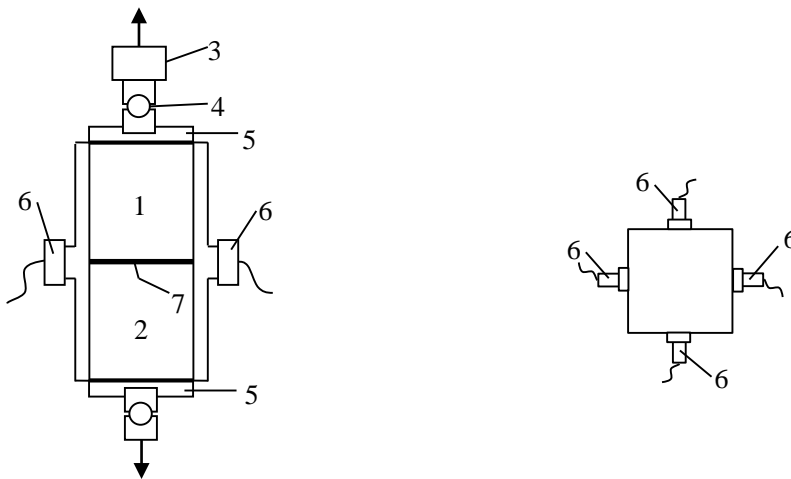
(b) Natural surface

529

530

Fig. 2. Test for obtaining the natural surface of rock

531



532

(a) Vertical view

(b) Plan view

533

1-concrete; 2-rock; 3-load cell; 4-ball joint; 5-steel plate; 6-clip; 7-interface

534

535

Fig. 3. Direct tensile test

536

537

538



539

(a) Artificial grooving interface

(b) Natural interface

540

541
542
543
544

Fig.4. Cracking patterns of rock-concrete interface



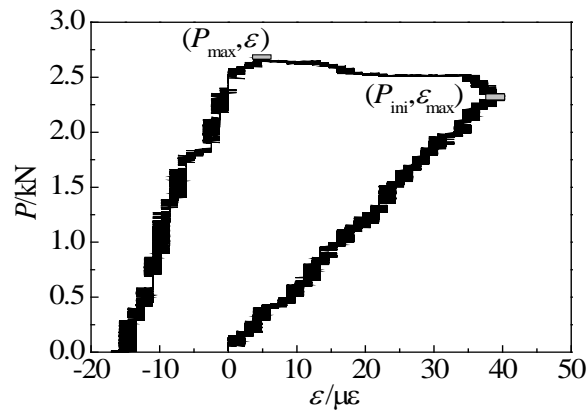
545
546
547

(a) Set-up for measurement of loading-point displacement

(b) Set-up for measurement of crack opening displacement

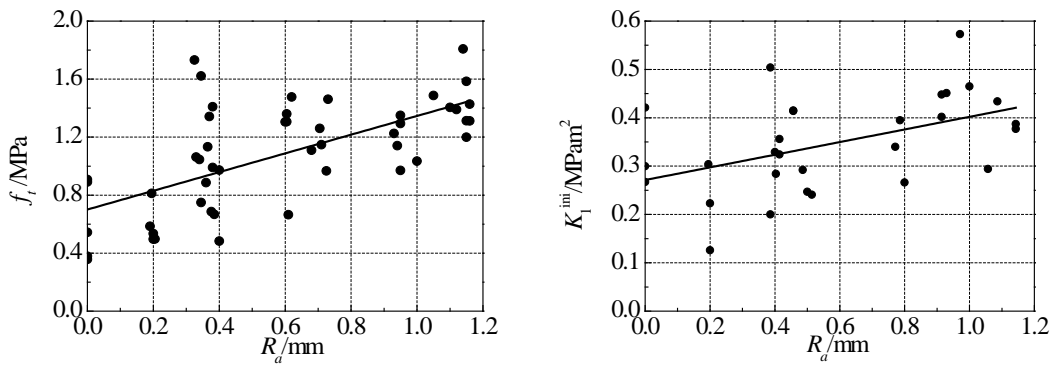
548
549

Fig. 5. Three-point bending beam test setup



550
551
552

Fig. 6. Strain variation of concrete around crack tip



553

554

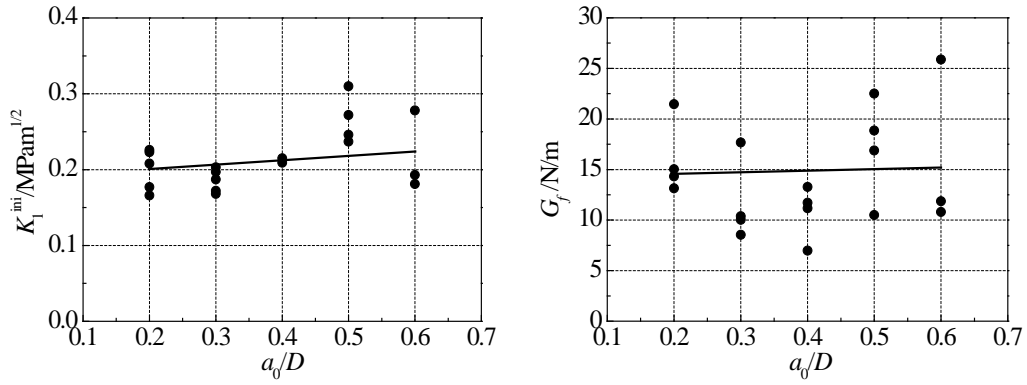
(a) Uniaxial tensile strength f_t

(b) Initial fracture toughness K_1^{ini}

555

Fig. 7. Effects of interface roughness R_a on f_t and K_1^{ini}

556



557

(a) Initial fracture toughness K_1^{ini}

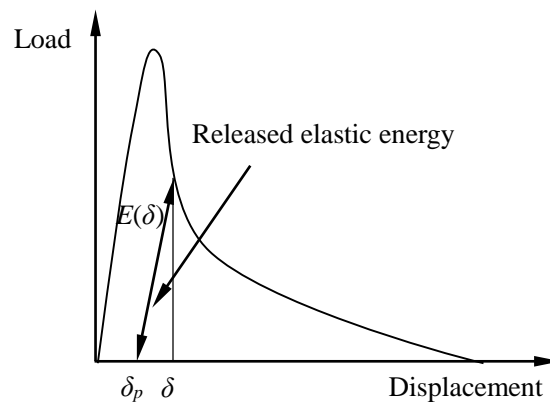
(b) Fracture energy G_f

558

559

Fig. 8. Effects of initial crack ratios a_0/D on f_t and K_1^{ini}

560



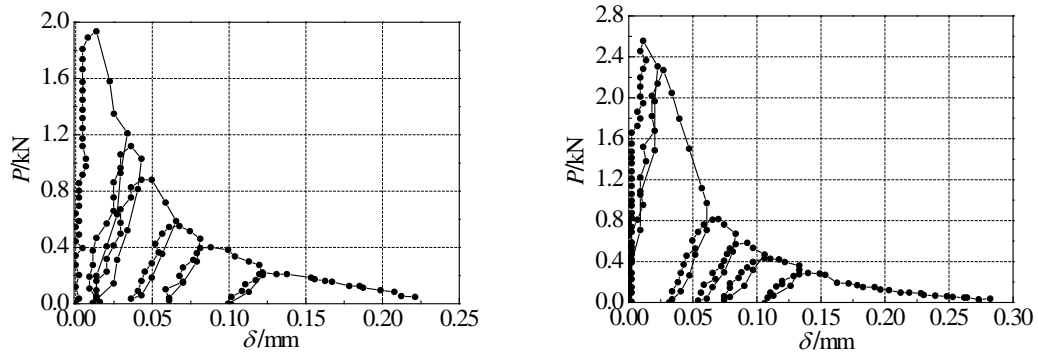
561

Fig. 9. Illustration of the modified J-integral method

562

563

564

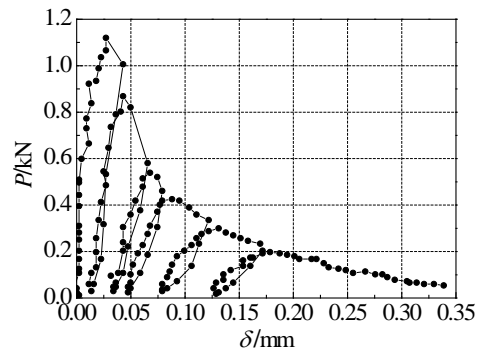
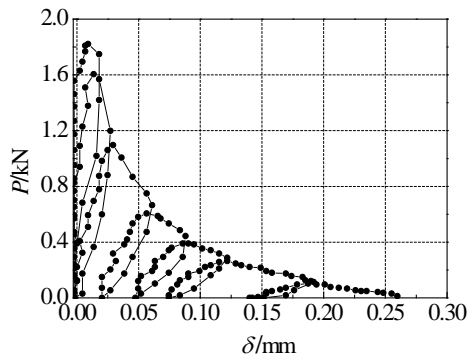


565

566

(a) TPB-A 4-2-3

(b) TPB-A 6-4-1



567

568

(c) TPB 2-5

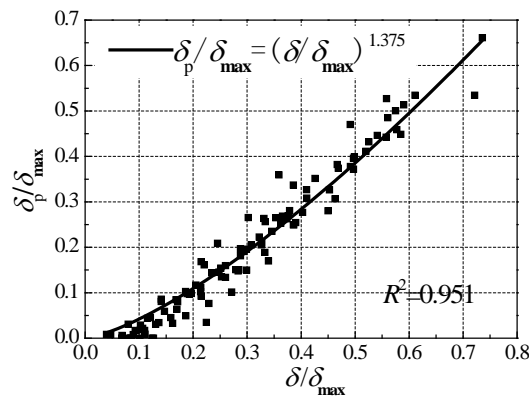
(d) TPB 5-5

569

Fig. 10. Load-displacement relationship

570

571



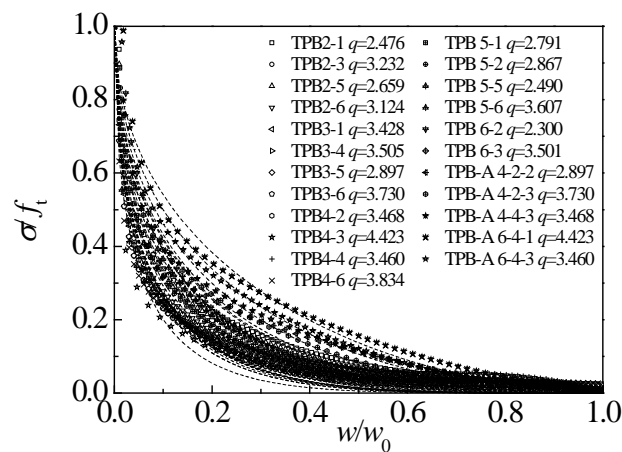
572

573

574

575

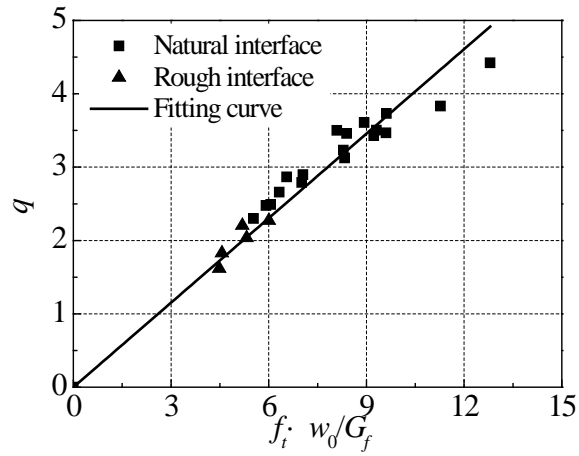
Fig. 11. δ_p/δ_{max} - δ/δ_{max} relationship



576

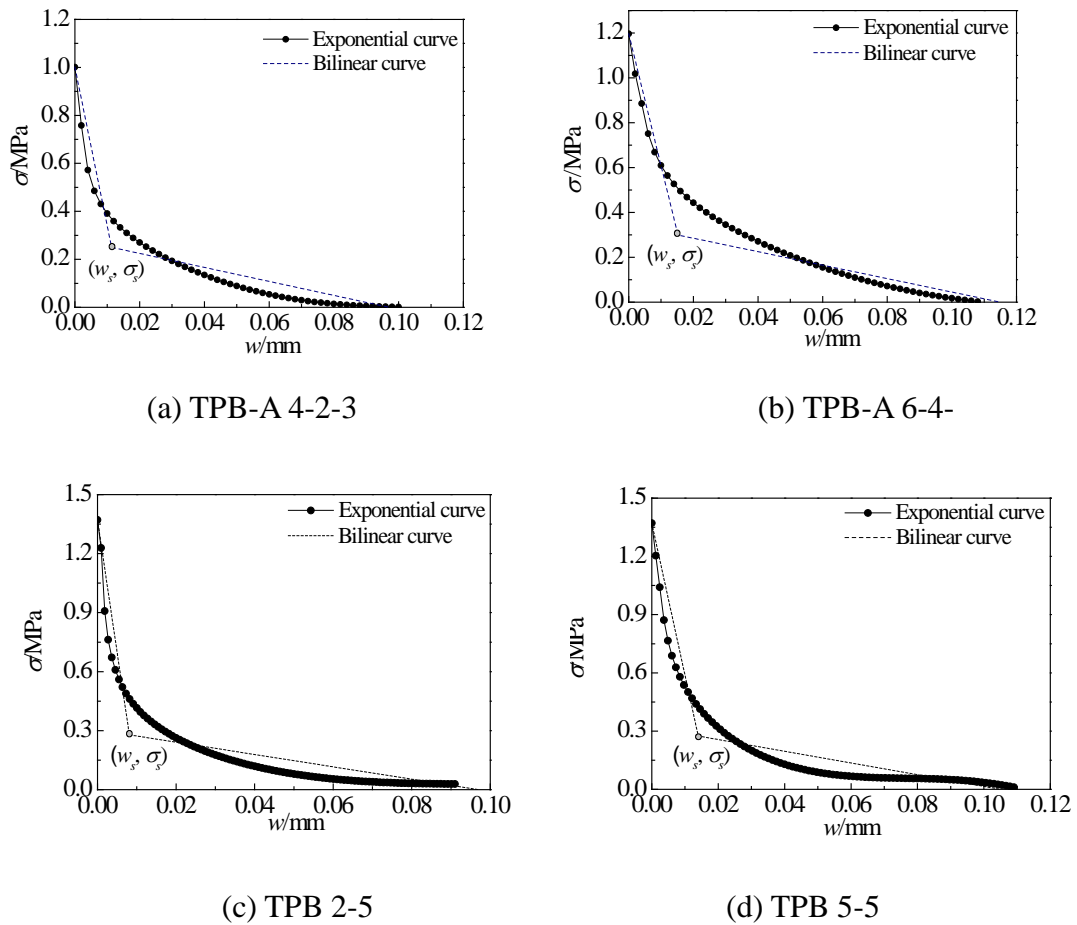
577
578
579

Fig. 12. $\sigma/f_t-w/w_0$ relationship



580
581
582
583
584

Fig. 13. Curve fitting for the material constant q

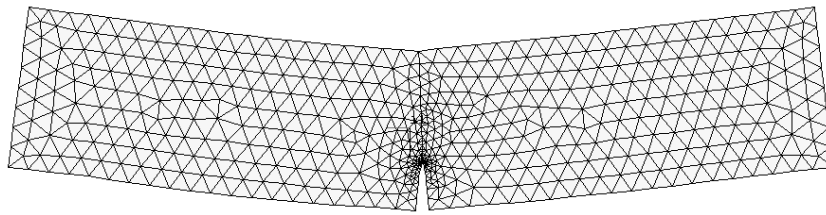


585
586
587
588
589

Fig. 14. Tension-softening constitutive law of rock-concrete interface

590

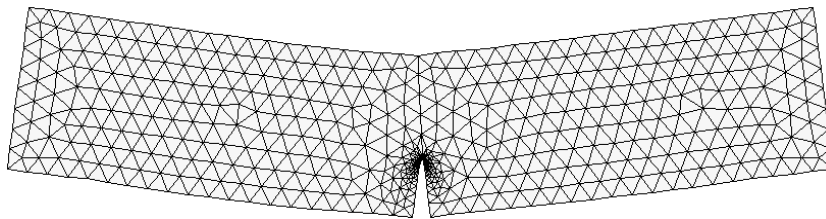
591



592

593

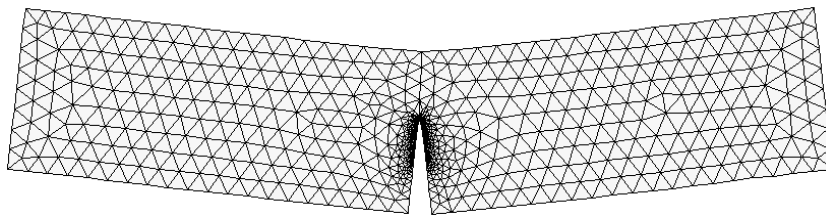
(a) Crack initiation



594

595

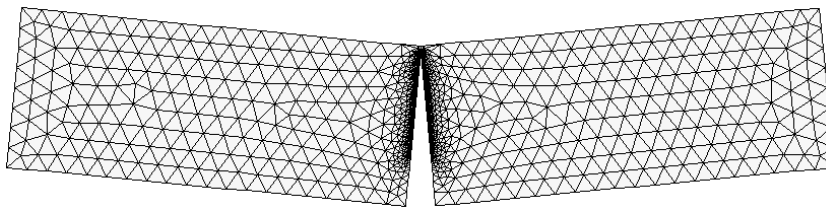
(b) Critical crack propagation (Peak load)



596

597

(c) The 15th increase step ($\Delta a=30\text{mm}$)



598

599

(d) Failure of specimens

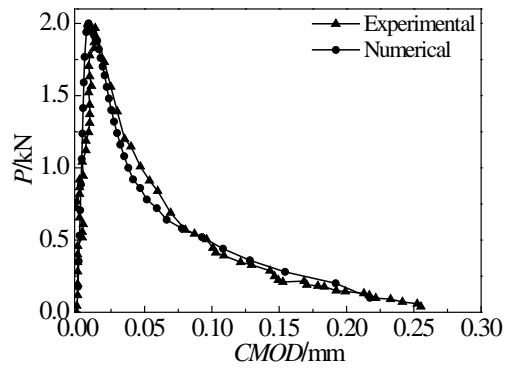
600

Fig. 15. Mesh and deformation of different fracture stages for specimen of TPB-A 4-2-3

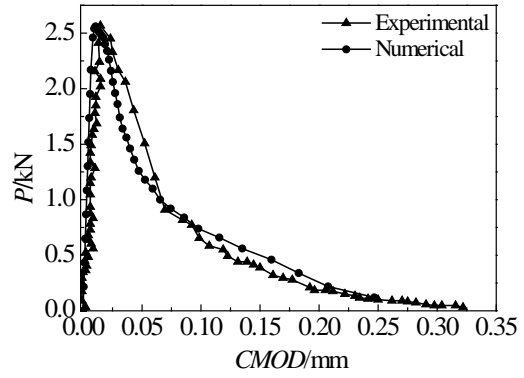
601

602

603



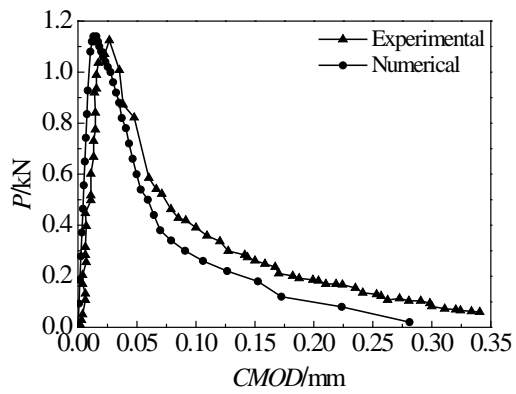
604



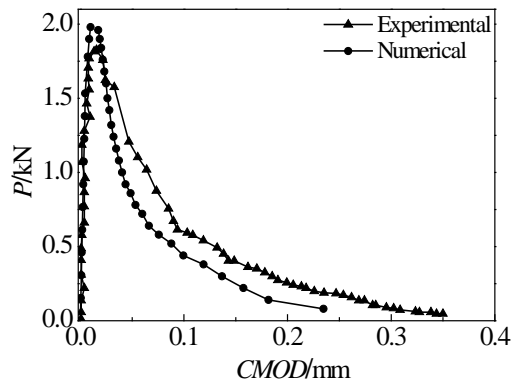
605

(a) TPB-A 4-2-3

(b) TPB-A 6-4-1



606



607

(c) TPB 2-5

(d) TPB 5-5

608

Fig. 16. *P-CMOD* curves obtained from experiment and numerical simulation

609

610

611

612

613

614

615

616

617

618

619